PNAS RESEARCH ARTICLE | EVOLUTION

Mosaic phenotypic evolution underlies the adaptive success of water-surface colonization in Gerromorpha

Zezhong Jin[a,1], Mu Qiao[a,1], Siying Fu[a], Zihe Li[a], Boxiong Guo[a], Hongjiao Li[a], Zhaoqi Leng[a,b], Matthew R. Pintar[c], Jakob Damgaard[d], Benjamin L. Makepeace[e], Silvia A. Mazzucconi[f], Gavril Marius Berchi[g], Fabio Cianferoni[h,i], Dan A. Polhemus[j], Kohei Watanabe[k], Jun Nakajima[l], Seraphine Esemu[m], Chen Liu[a], Beichen Zhang[a], Huanhuan Yang[n], Shujing Wang[a], Huaijun Xue[a], Wenjun Bu[a,2], and Zhen Ye[a,2]

Affiliations are included on p. 11.

Edited by Geerat Vermeij, University of California Davis, Davis, CA; received November 28, 2025; accepted February 3, 2026

Understanding how the remarkable phenotypic diversity observed in organisms arises through shifts in macroevolutionary patterns and tempos is a fundamental challenge in evolutionary biology. Phenotypes often evolve in a mosaic pattern during adaptive transitions. For organisms that have invaded highly specialized habitats, such as the unique two-phase interface habitats (water surfaces), the macroevolutionary history of their phenotypic diversification remains only superficially understood. Semiaquatic bugs (Insecta: Heteroptera: Gerromorpha), which exhibit extensive habitat diversification and unparalleled phenotypic innovation, represent one of the most successful extant adaptive groups at this interface and provide an excellent system for study. By analyzing their adaptive transitions and phenotypic macroevolutionary history, we demonstrate that Gerromorpha experienced a single major adaptive transition from land to the water surface. Subsequently, semiaquatic bugs successfully colonized a wide range of distinct water-surface habitats. During this process, phenotypic space was explored under strong constraints and along pronounced mosaic trajectories; i.e., different body regions exhibited markedly distinct patterns of phenotypic space occupation and partitioning, as well as markedly different evolutionary rates. Furthermore, we showed that this mosaic pattern of phenotypic space occupation and rates of exploration had complex and critical effects on the invasion and colonization of water-surface habitats. Our study provides a typical case of macroevolutionary dynamics in species adapted to specialized air–water interface habitats, emphasizing the complex and significant roles of environmental context and functional demands in shaping patterns of phenotypic evolution.

diversification | phylogeny | phenotypic evolution | mosaic evolution | Gerromorpha

Adaptive radiation refers to the rapid diversification of a lineage in response to a new ecological opportunity and is typically characterized by both rapid lineage diversification and the attainment of peak morphological disparity rapidly in the early stage of clade's evolutionary history (1–4). Increasing evidence suggests that phenotypic evolutionary patterns associated with ecological adaptation often exhibit mosaic configurations. These patterns integrate heterogeneous evolutionary rates and directions across different anatomical regions, indicating that adaptive radiation may proceed primarily along specific ecomorphological axes rather than spanning the entire phenotypic space (5–10). This mosaic pattern is frequently invoked to explain the adaptive evolutionary processes of organisms throughout their habitat-occupation history, highlighting the unique evolutionary trajectories exhibited by parts of the organism that directly interact with the environment. For instance, land birds show greater evolutionary disparities in elements such as the mandible and tarsometatarsus, whereas water birds exhibit more significant differences in the femur and tibiotarsus, which are associated with the lever mechanics of water birds (5). Therefore, organisms that modify their modes of interaction with the environment and colonize novel habitats provide an excellent framework for investigating the mosaic macroevolutionary history of phenotypes. Exciting research has been conducted on the earliest tetrapods from water to land (11, 12) and subsequent processes of the multiple independent invasions into the oceans (13) or skies (14, 15). Given the substantial differences in physical environments, such macroevolutionary studies often focus on physical phase-to-phase transitions—for example, from land to water—which represent adaptive evolutionary processes under conditions of drastic environmental change. However, species that permanently colonize the interfaces between phases, such as the air–water interface or the water–solid interface, have generally received less attention. Some studies have been carried out on benthic fishes, for example (16, 17). These species that inhabit "interface" environments are subject to distinctive environmental constraints, and their

Significance

Currently, our understanding of the macroevolutionary history of organisms that have colonized highly specialized two-phase habitats, such as air–water interfaces, remains rudimentary. Semiaquatic bugs (Insecta: Heteroptera: Gerromorpha), which exhibit extensive habitat diversification and unparalleled phenotypic innovation, represent one of the most successful extant adaptive groups at this interface, offering a valuable system for study. Here, we reconstructed a representative history of colonization in water-surface habitats and demonstrate that this process was characterized by a distinctly mosaic phenotypic macroevolutionary pattern, which played a complex and critical role in the occupation of diverse water-surface habitats. Incorporating these insights into macroevolutionary models will help deepen our understanding of the intricate relationships between environmental context and the exploration of phenotypic space.

The authors declare no competing interest.

This article is a PNAS Direct Submission.

[1]Z.J. and M.Q. contributed equally to this work.

[2]To whom correspondence may be addressed. Email: wenjunbu@nankai.edu.cn or yezhen1987331@nankai.edu.cn.

This article contains supporting information online at https://www.pnas.org/lookup/suppl/doi:10.1073/pnas.2534611123/-/DCSupplemental.

Published March 12, 2026.

phenotypic macroevolutionary histories remain crucial for deepening our understanding of the adaptive radiation and mosaic evolution processes.

The air–water interface represents a particularly distinctive set of ecological habitats, characterized by hydrodynamic constraints that limit the locomotion of most taxa at this surface. Organisms that float here rely on the surface tension of the capillary interface for support and movement, and counteracting fluid resistance (18, 19). The widely studied basilisk lizard, for instance, can run across the water surface by generating sufficient supporting forces with its feet (20, 21); however, it is unable to permanently inhabit this environment. In contrast, certain specialized semiaquatic arthropods—such as whirligig beetles, fishing spiders, and water striders—have been evolving for over 100 My and have successfully colonized this interface (18, 19, 22). Among them, semiaquatic bugs (Insecta: Hemiptera: Heteroptera: Gerromorpha) represent the most successful group adapted to life on the surface of water (22). These bugs occupy a wide range of habitats, spanning from humid land to freshwater surfaces and even the open ocean surfaces. Some lineages are capable of inhabiting the surface of fast-flowing turbulences and have exhibited remarkable phenotypic variations during adaptive evolution on the water surface (22–24). For example, larger-bodied species often evolve disproportionately elongated middle legs specifically adapted for rowing, while other lineages exhibit extreme miniaturization, allowing them to achieve agile locomotion with short legs (22). Evidence suggests that the ancestors of Gerromorpha were terrestrial and successfully adapted to the water surface through a series of key evolutionary transitions (22, 25). This remarkable shift has positioned Gerromorpha as a focal group for evolutionary biologists. Significant advances have provided substantial insights into the adaptive physical mechanisms, morphological traits, and molecular mechanisms underlying their evolutionary success (26–35). Moreover, extensive research has been devoted to elucidating the phylogeny and adaptive evolutionary history of this group (25, 36–42). These studies, spanning various taxa, have gradually enhanced our understanding of the tree of life for Gerromorpha. A recent phylogenetic analysis employing transcriptomic markers has provided a relatively comprehensive framework for understanding the phylogenetic relationships (25) within Gerromorpha and has addressed several pivotal evolutionary questions, including the evolution of locomotion modes, sexual selection, adaptations to saltwater invasion, and wing polymorphism (25). Nevertheless, debates regarding phylogenetic relationships persist, primarily due to the absence of key groups. Meanwhile, due to the lack of comprehensive phenotypic and ecological datasets, the patterns of phenotypic adaptive evolution in Gerromorpha, especially whether the appendages that interact directly with the environment exhibit a mosaic evolution process, remain unexplored.

Given the highly distinctive adaptive transition process to the water surface, the diverse habitat occupation, the pronounced phenotypic disparity, and the long evolutionary history of this group (22), integrating multidimensional phenotypic datasets and a more comprehensive phylogenetic framework is essential to investigate how these semiaquatic insects have successfully colonized diverse water-surface habitats. This exploration should also examine the complex modes and tempo of their occupation of phenotypic space, and the role of phenotypic-space exploration in driving adaptive shifts. This will enhance our understanding of the macroevolutionary processes that underlie the adaptation of all taxa to the water surface, a uniquely two-phase environment.

To this end, we reconstructed the most comprehensive species-level phylogenetic framework for Gerromorpha to date and integrated extensive habitats information alongside continuous and discrete phenotypic datasets to assess the adaptive history of phenotypic space occupation. Building upon this consolidated dataset, we aimed to address three core questions: 1. What is the typical history of invasion into an extremely specialized two-phase interface and the subsequent occupation of diversified habitats? 2. During these special processes of adaptive transition, do the elements that interact with the environment exhibit a mosaic evolutionary pattern of occupation in phenotypic space? 3. How important are positional occupancy and evolutionary rate along different phenotypic axes for these particular adaptive transition processes?

Results

Phylogenetic Relationships of Gerromorpha. The reconstructed phylogenetic topologies across all datasets demonstrated a high degree of congruence among the diverse analytical approaches and models employed, with only minor discrepancies observed at a few nodes (*SI Appendix*, Figs. S2 and S3). The monophyly of Gerromorpha, the family Hermatobatidae, the clade (Mesoveliidae + Hebridae + Paraphrynoveliidae + "Hydrometridae" + "Macroveliidae"), the clade ("Veliidae" + Gerridae), and the family Gerridae was consistently supported with high support values (*SI Appendix*, Fig. S2). Nevertheless, some family-level and subfamily-level taxa were found to be paraphyletic (*SI Appendix*, Figs. S2 and S3 and *Supplementary Results*). While some inconsistencies persist in certain clades, the overall phylogenetic topology aligns closely with the results of Armisén et al. based on transcriptome data (25). The phylogenetic topology inferred from the mitoPCG_123+18S28S+UCE dataset was ultimately adopted for all subsequent analyses.

Divergence Time of Gerromorpha. Divergence time estimates for most nodes within Gerromorpha, as determined using MCMCTREE, were largely consistent with those obtained from r8s analyses (*SI Appendix*, Table S5). The 95% highest posterior density (HPD) intervals from MCMCTREE and the CI derived from 100 trees in the r8s analyses for these key temporal estimates are summarized in *SI Appendix*, Table S5. The origin of Gerromorpha is estimated to have occurred around the Permian–Triassic boundary, approximately 247 Mya (95% HPD: 231.33 to 262.33 Mya) (Fig. 1 and *SI Appendix*, Table S5). The family Hermatobatidae diverged from other gerromorphan species during the Lower Jurassic, around 193 Mya (95% HPD: 174.45 to 211.16 Mya) (Fig. 1 and *SI Appendix*, Table S5). Two main clades, namely clade (Mesoveliidae + Hebridae + Paraphrynoveliidae + "Hydrometridae" + "Macroveliidae") and clade (Gerridae + "Veliidae"), diverged during the Lower Jurassic, approximately 179 Mya (95% HPD: 162.98 to 196.14 Mya), with further diversification occurring during the Middle Jurassic (Fig. 1 and *SI Appendix*, Table S5). The diversification of the major lineages was concentrated between the Middle Jurassic and Upper Cretaceous, spanning approximately 160 to 79 Mya (Fig. 1 and *SI Appendix*, Table S5).

Habitats Occupation History of Gerromorpha. Following Andersen's concepts and terminology (22), we identified eight typical habitat types for Gerromorpha. Considering potential interlineage heterogeneity in habitat transition rates, we introduced evolutionary models both with and without hidden rate categories. After maximum-likelihood estimation under the best-fit model, we identified two categories of instantaneous transition rates that differed by nearly two orders of magnitude among habitat-occupation states in the history of adaptive shifts (*SI Appendix*, Fig. S4 and

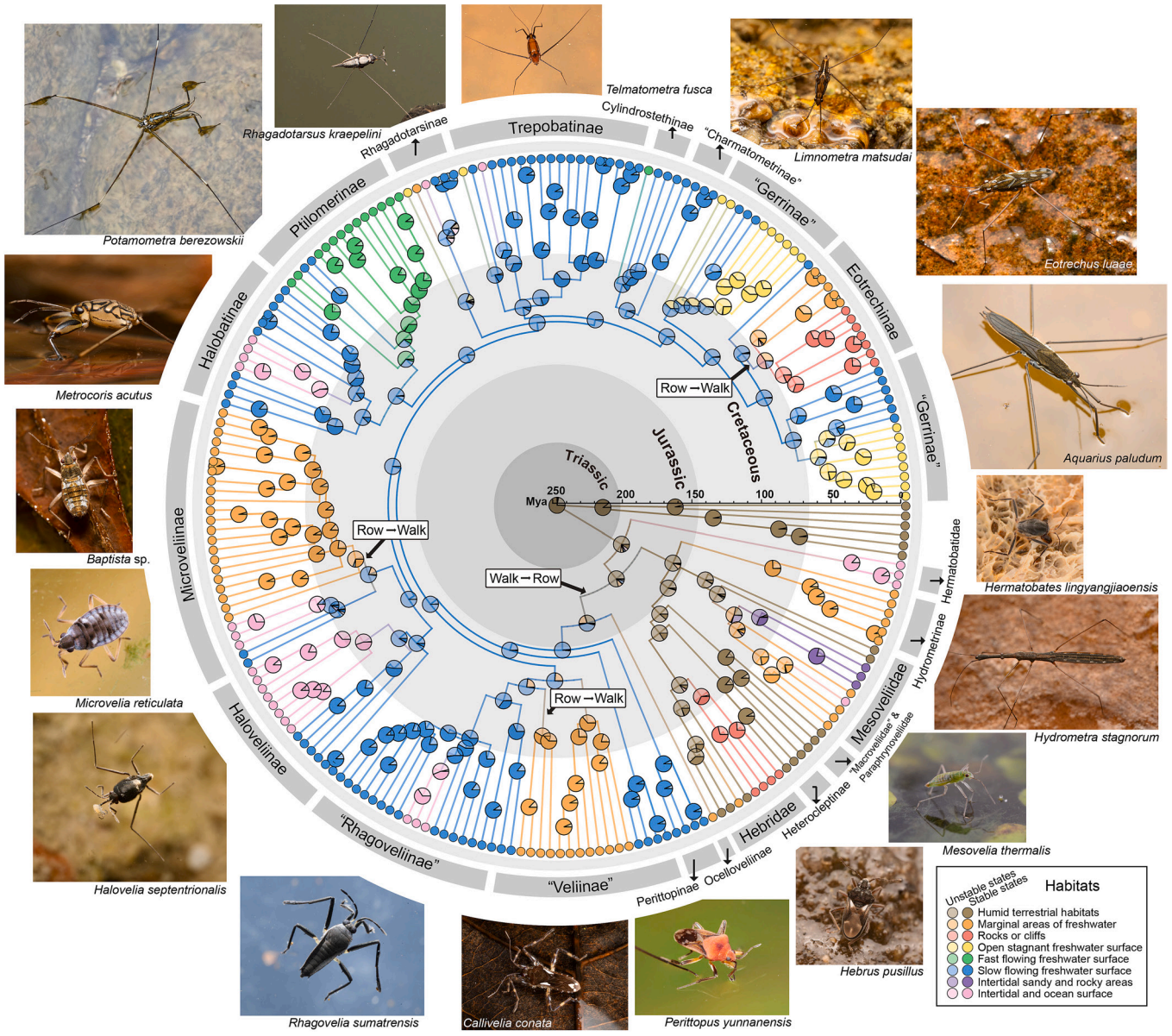

Fig. 1. Adaptive colonization history of water-surface habitats in Gerromorpha. Lighter colors indicate unstable occupation stage, characterized by relatively high instantaneous transition rates among habitat categories, whereas darker colors indicate stable occupation stage, with very low instantaneous transition rates among habitat categories. Reconstructed locomotion modes are mapped onto key nodes. Representative live habitus of Gerromorpha spp. in situ are displayed in the outer ring.

Table S6). We defined the higher-rate category as unstable habitat-occupancy states (i.e., states that readily transition among habitats; shown with lighter colors) and the lower-rate category as stable habitat-occupancy states (i.e., states in which habitat occupancy is relatively persistent and unlikely to shift; shown with darker colors) (Fig. 1 and *SI Appendix*, Fig. S4). Ancestral state reconstruction supports the hypothesis that Gerromorpha originated in humid terrestrial habitats, which aligns with findings from previous studies (22, 37, 38), after which two principal adaptive strategies emerged (Fig. 1). The basal main clade, comprising Mesoveliidae, Hebridae, Paraphrynoveliidae, "Hydrometridae," and "Macroveliidae," retained ancestral adaptations throughout its evolutionary lineage, without major habitat shifts from land to water surface (Fig. 1). In contrast, another main clade, comprising Gerridae and "Veliidae," underwent a remarkable habitat shift from land to water surface, occupying diverse water-surface habitats in a very short period (Fig. 1 and *SI Appendix*, Fig. S5). These included open stagnant freshwater surfaces, fast-flowing turbulent water surfaces, and intertidal and oceanic surface habitats (Fig. 1 and *SI Appendix*, Fig. S5). Multiple independent invasions into different habitats have occurred repeatedly and are widespread across the entire phylogeny of Gerromorpha, aligning with inferences from previous studies (22, 25, 39–41) (Fig. 1 and *SI Appendix*, *Supplementary Results*). Across the entire phylogeny of Gerromorpha, diversification in habitat occupancy occurred during the early unstable habitat-occupancy stage, followed by a shift to stable occupation within each habitat. Transitions between habitat-occupation states became rare over time (Fig. 1). In summary, the habitat-occupation history of Gerromorpha is both highly complex and relatively ordered.

Diversification Rates. The Bayesian Analysis of Macroevolutionary Mixture (BAMM) analysis revealed heterogeneity in speciation, extinction, and net diversification rates (*SI Appendix*, Fig. S6). Speciation and net diversification rates exhibited an overall increase throughout the evolutionary history (*SI Appendix*, Fig. S6). Notably, significant differences in diversification rates

were observed among species inhabiting different habitats (*SI Appendix*, Fig. S6 and Table S9). For example, species occupying terrestrial habitats (including humid terrestrial, intertidal sandy, and rocky areas) exhibited lower speciation, extinction, and net diversification rates which were significantly different from those of species inhabiting other habitats (*SI Appendix*, Fig. S6 and Table S9). In contrast, species inhabiting various water-surface habitats displayed no significant rate differences (*SI Appendix*, Fig. S6 and Table S9).

Occupation Patterns of Phenotypic Space. The relative lengths of appendage segments exhibited a strong and significant phylogenetic signal, indicating that their evolutionary patterns align closely with the phylogenetic relationships (*SI Appendix*, Table S10). Given this, and the proportions of phenotypic variance explained by the principal component axes (*SI Appendix*, Fig. S7 and Table S11), the results of the PaCA were used to reparameterize the overall phenotypic space for subsequent analyses. The relative lengths of middle leg segments were found to have the highest loads on PC1 axis (*SI Appendix*, Table S12).

The overall phenotypic space of continuous traits for extant species reveals significant adaptive partitioning across different habitats (Fig. 2 and *SI Appendix*, Fig. S8). Species occupying water-surface habitats exhibit substantial phenotypic differentiation when compared to species occupying terrestrial habitats, characterized by low overlap, large unique fraction, and large spatial distances within phenotypic-space hypervolumes (Fig. 2 and *SI Appendix*, Fig. S9 and Table S13). Species inhabiting different water-surface habitats also show distinct spatial partition patterns (Fig. 2 and *SI Appendix*, Figs. S8 and S9 and Table S13). The most special case is the fast-flowing water surfaces, where species occupying this habitat occupy extreme positions in phenotypic space, exhibiting significant differences from all other habitats, with minimal overlap, the maximal proportion of unique fractions, and large spatial distances (Fig. 2 and *SI Appendix*, Figs. S8 and S9 and Table S13). The overlaps between the phenotypic spaces of species from habitats that have been independently invaded multiple times and those of species from their corresponding source habitats, as well as the strength of convergence (quantified by the C1–C4 indices), also exhibit differences (Fig. 2 and *SI Appendix*, Figs. S9 and S10, Tables S13 and S15, and *Supplementary Results*).

On the temporal scale, the overall phenotypic space also exhibits a similar occupation. Following the initial colonization of water-surface habitats, phenotypic trajectories of species diverged and progressively distanced away from those of their terrestrial counterparts (Fig. 2). Species inhabiting fast-flowing water surfaces consistently occupy extreme phenotypic positions (Fig. 2). This partitioning of phenotypic space among habitats was established during the unstable habitat-occupation stage and persisted into the stable stage (*SI Appendix*, Fig. S12 and Table S14).

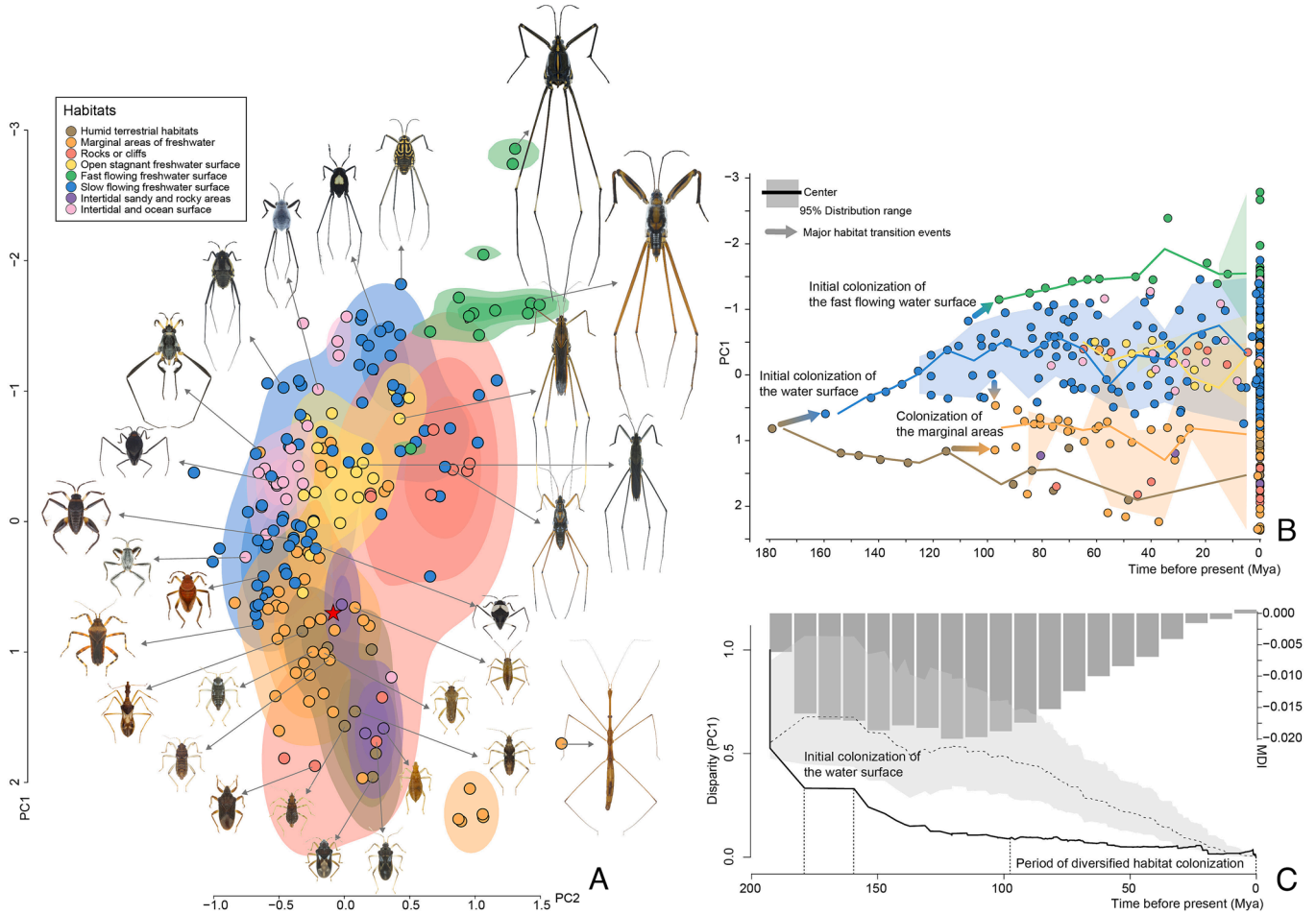

Fig. 2. Overall phenotypic space partitioning and evolutionary history of Gerromorpha across different habitat occupations. (*A*) Habitat partitioning of the overall phenotypic space of extant species, shown along the first two principal component axes from the PaCA. The red star represents the position of the root node in the phenotypic space. (*B*) Temporal trajectory of overall phenotypic variation, represented by the first principal component axis from the PaCA, together with major adaptive shift events. (*C*) Disparity-through-time pattern of overall phenotypic variation. The black line indicates the empirical disparity; the light-gray band indicates the expected disparity interval from 1,000 simulations; and the dark-gray bars represent the difference between empirical disparity and the mean expected disparity for each time bin, i.e., the MDI.

During this process, species in each habitat-occupation type further explored their phenotypic space, with this pattern being particularly pronounced among species occupying freshwater-surface habitats (*SI Appendix*, Fig. S12, Table S14, and *Supplementary Results*). Although some adaptive exploration was observed, it remained constrained compared to a neutral Brownian motion (BM) process, as evidenced by consistently low morphological disparity indices (MDI, Fig. 2*C*). The initial invasion from land to water-surface habitats did not relax this constraint; only during the subsequent phase of habitat diversification did exploration of phenotypic space begin to increase, albeit in a limited manner (Fig. 2).

Mosaic Evolutionary Patterns across Phenotypic Axes in Habitat Diversification and Colonization History. For Gerromorpha species, the exploration history of body length and individual appendage segments is mosaic, characterized by differences in the degree of constrained exploration (Fig. 3 and *SI Appendix*, Fig. S14 and Table S16) and evolutionary rates over time (*SI Appendix*, Figs. S17 and S18), as well as different strengths of convergence across habitats (*SI Appendix*, Tables S15). For instance, locomotion-related appendages, such as segments of the middle legs, remain strongly constrained, as indicated by negative MDI values (Fig. 3 and *SI Appendix*, Fig. S14 and Table S16), lower evolutionary rates (*SI Appendix*, Fig. S18), and pronounced convergence across multiple habitats (*SI Appendix*, Table S15). This exploration pattern contrasts with other phenotypic axes, especially the antennal segments (Fig. 3 and *SI Appendix*, Figs. S14 and S18 and Tables S15 and S16).

In the early stage of unstable habitat occupation and diversification, significant differences in positional occupations along multiple phenotypic axes were observed among habitat-occupancy groups, particularly between terrestrial and water-surface habitats (*SI Appendix*, Fig. S15 and Table S17). Species occupying water-surface habitats tended to occupy more extreme positions along several phenotypic axes, with this trend intensifying as habitat differentiation progressed (*SI Appendix*, Fig. S15 and Table S17). In contrast, during this stage, evolutionary rates across phenotypic axes did not exhibit widespread variations and were not specifically concentrated in comparisons between terrestrial and water-surface habitats (*SI Appendix*, Fig. S20 and Table S21). From the unstable to the stable stage of habitat colonization, the positional distributions along individual phenotypic axes did not show significant bias, although some range of expansion was observed (*SI Appendix*, Fig. S16 and Table S18). Evolutionary rates for several phenotypic traits became significantly biased toward lower values (*SI Appendix*, Fig. S21 and Table S22), leading to widespread differences in phenotypic evolutionary rates among extant species occupying different habitats (*SI Appendix*, Fig. S19 and Table S20). These results suggest that the spatial partitioning along each phenotypic axis was established at an early stage, consistent with the patterns shown in Fig. 3. The subsequent reduction of evolutionary rates on certain phenotypic axes in specific habitats during the habitat-stabilization stage led to cross-axis heterogeneity in evolutionary rates. LASSO regression results for phenotypic evolution rates and species diversification rates revealed that the influence of phenotypic evolution rates on diversification rates underwent complex changes during the water-surface habitat diversification and stable colonization process (*SI Appendix*, Fig. S22, Tables S23 and S24, and *Supplementary Results*).

Given the mosaic pattern of phenotypic space occupancy described above, we employed the random-forest model to evaluate the relative importance of complex, nonlinear differences across each phenotypic axis during major habitat colonization processes. The mosaic distribution patterns of spatial occupancy across different phenotypic axes and evolutionary rates exhibit complex and uneven contributions during different stages of habitat

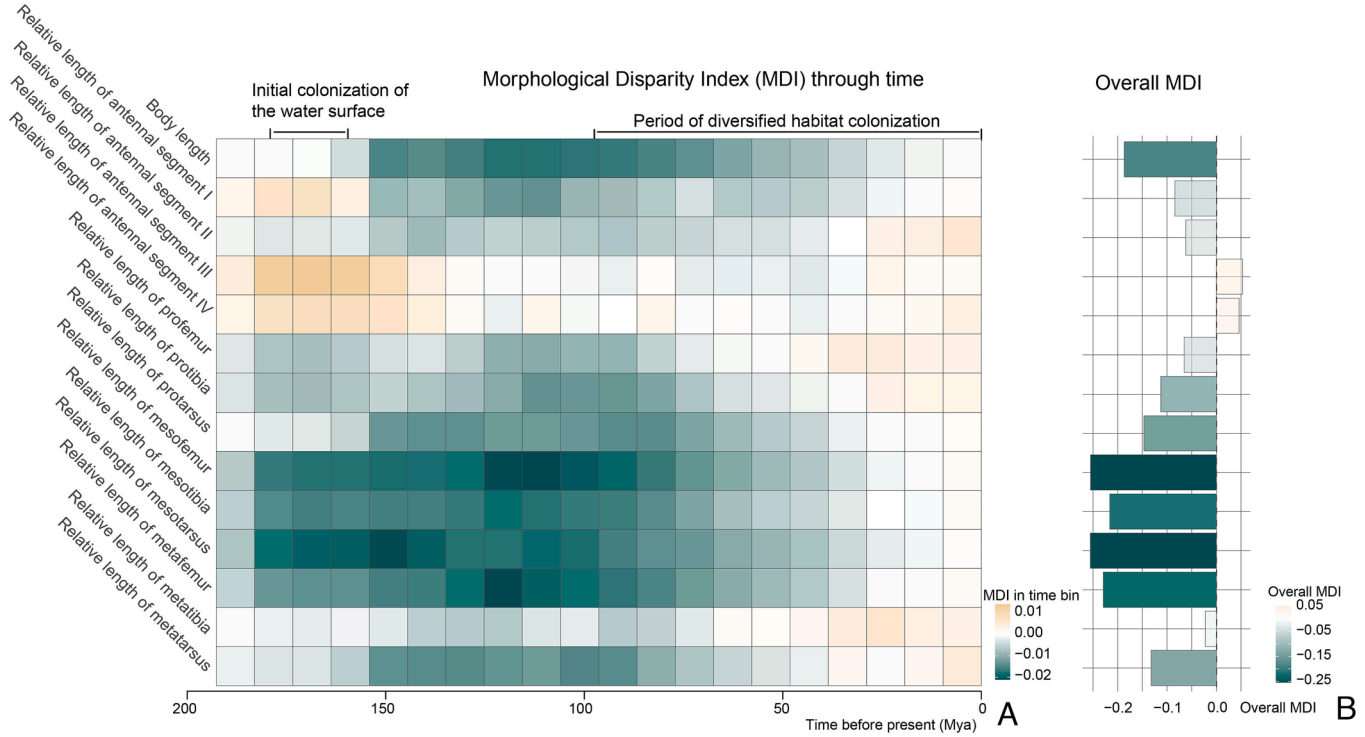

Fig. 3. The temporal dynamics of phenotypic space exploration along different phenotypic axis of Gerromorpha, demonstrated using the MDI. (*A*) MDI defined as the difference between the observed morphological disparity and the average disparity expected under a random BM model. The heatmap colors represent MDI values within each of 20 equally spaced time slices along the time axis: negative values (green) indicate constrained exploration of phenotypic space, whereas positive values (yellow) indicate more extensive exploration of phenotypic space. (*B*) Overall MDI through time for different phenotypic axes.

diversification and stable colonization (Fig. 4 and *SI Appendix*, Tables S25–S28). Some traits, such as middle leg segments directly related to locomotion, exhibited significant importance during the initial land-to-water transition, occupying regions with larger values on these axes (Fig. 4 and *SI Appendix*, Fig. S15). However, the evolutionary rates of these traits were less important compared to other phenotypes, such as antennal segments, which exhibited differences (Fig. 4 and *SI Appendix*, Fig. S20). Furthermore, the positional occupancies and evolutionary rates of the segments of middle leg showed differential importance during subsequent diversification in water-surface habitats and stable occupancy within these habitats (Fig. 4 and *SI Appendix*, Tables S25–S28). This suggests that, at least along certain phenotypic axes, spatial position may be more important than the spatial exploration rate during adaptive transitions. Similarly, the positional occupancies and evolutionary rates of body length, antennal segments, and segments of the fore and hind legs exhibited unique importance across different habitat-occupancy stages (Fig. 4 and *SI Appendix*, Tables S25–S28).

Accumulation of Discrete Phenotypic Innovations and Evolution of Locomotion Patterns across Different Habitats. We quantified cumulative discrete trait innovations in species from different habitats, relative to the reconstructed root state, under the best-fit evolutionary model for each phenotypic dataset (*SI Appendix*, Table S29). In terrestrial habitats, cumulative innovations were generally low, whereas most water-surface habitats showed elevated levels (*SI Appendix*, Fig. S23). Ancestral reconstruction of locomotion modes indicated a major shift from "walking" to "rowing" during the transition from land to water, followed by multiple reversals from "rowing" back to "walking" in marginal habitats (Fig. 1). In contrast, species in open water-surface habitats retained the same locomotion mode throughout their evolutionary history (Fig. 1).

Discussion

The diverse and habitat-specialized species within the infraorder Gerromorpha offer valuable insights into macroevolutionary processes in successful colonizers of interface habitats. Integrating of macroevolutionary phylogenetic analyses with multi-trait phenotypic data provides compelling evidence for a complex, mosaic pattern of evolution across various phenotypic axes during the successful invasion and stable colonization of diverse water-surface habitats by Gerromorpha. Such a mosaic pattern of phenotypic evolution is likely characteristic of the occupation of these specialized habitats.

The Phylogeny of Gerromorpha. The phylogenetic relationships among families and subfamilies within Gerromorpha have long been debated. In this study, we address previous sampling limitations by incorporating specimens from key groups such as "Macroveliidae," Paraphrynoveliidae, and Ocelloveliinae, thereby providing the

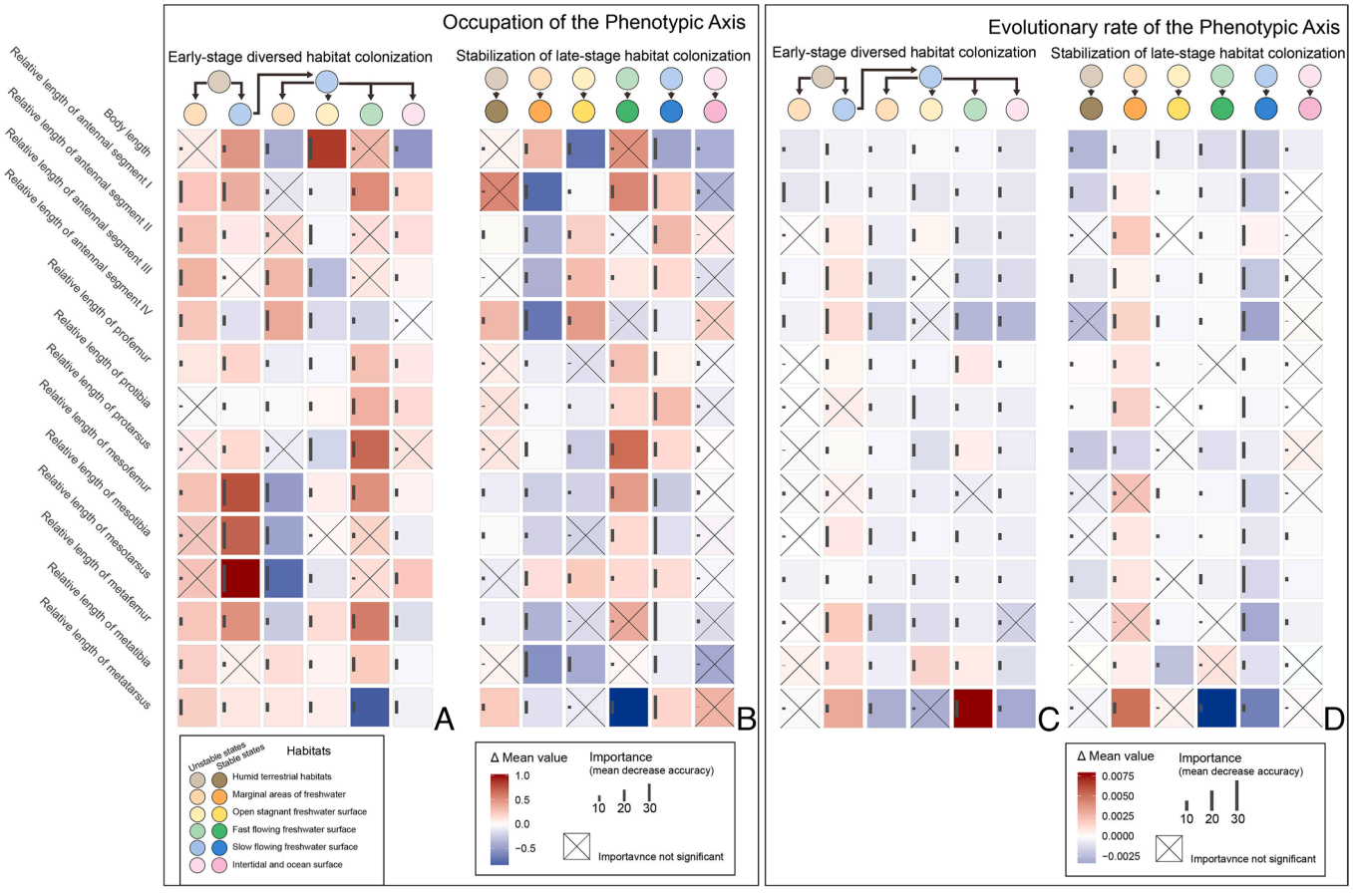

Fig. 4. Importance of positional occupation and evolutionary rates across phenotypic axes during major habitat transitions and stable occupation stages. The importance values were quantified by the MDA from random-forest models. Lighter colors within the circles above indicate unstable habitat occupation stage, whereas darker colors indicate stable occupation stage. Heatmap colors represent differences in mean values across processes, and the length of the dark gray bar on the left side of each cell denotes the MDA values. Statistical significance of importance was assessed using 2,000 permutation tests and the cells that do not reach the significance threshold (*P*-value exceeded 0.05) are marked with a cross. (*A*) Mean value difference and importance of positional occupation in early-stage habitat colonization. (*B*) Mean value difference and importance of positional occupation in stabilization of late-stage habitat colonization. (*C*) Mean value difference and importance of evolutionary rate in early-stage habitat colonization. (*D*) Mean value difference and importance of evolutionary rate in stabilization of late-stage habitat colonization.

most accurate representation of phylogenetic relationships within the infraorder to date. Our findings indicate that a substantial taxonomic revision is needed, as many high-level taxa within Gerromorpha are paraphyletic. Several families were found to be recombinable, with "Macroveliidae" and Paraphrynoveliidae being supported as a unified family. Furthermore, "Hydrometridae" and "Veliidae" were strongly supported as paraphyletic groups, suggesting that they should be split in future classifications. The monophyly of certain subfamilies has also been questioned. A detailed discussion of the phylogeny of Gerromorpha can be found in *SI Appendix*, *Supplementary Discussions*.

The Adaptive Evolutionary History from Land to Water Surface. The Mesozoic Era is widely recognized as a prolonged greenhouse climate period (43, 44). The breakup of Pangaea significantly enhanced marine influence across numerous regions, resulting in a generally warmer and more humid climate (43–46). During this period, insects underwent significant radiative evolution, marked by the emergence and diversification of various ecological types (47). Fossil evidence suggests that the origin of Gerromorpha can be traced back to the Triassic (48). Our analyses align with fossil evidence and previous phylogenetic studies (25, 38, 49). The origin of Gerromorpha occurred near the Permian–Triassic boundary, with major lineage diversification concentrated between the Middle Jurassic and Upper Cretaceous (Fig. 1). Our results indicate that the overall speciation rate and net diversification rate of Gerromorpha has steadily increased (*SI Appendix*, Fig. S6). Furthermore, the first invasion of the water surface by Gerromorpha occurred during the Middle to Upper Jurassic, followed by habitat diversification and stable colonization from Cretaceous to the present (Fig. 1 and *SI Appendix*, Fig. S5). Biological factors likely contributed to this diversification. As gerromorphans primarily feed on other insects (22), the Mesozoic radiation of insects would have provided a diverse and abundant food source. Conversely, competition with the extinct Polyneopteran family Chresmodidae—a group of surface-skating insects from the Late Jurassic to Early Cretaceous—may have influenced diversification of Gerromorpha. Both groups shared similar ecological niches and were likely carnivorous, potentially leading to competitive interactions (50).

Several habitats experienced multiple independent invasion events occurring throughout the entire phylogenetic framework (Fig. 1). For instance, independent invasions of the "marginal areas of freshwater" habitat occurred within subclades predominately in the Upper Cretaceous (Fig. 1), and "intertidal areas and ocean surfaces" also experienced independent colonization within subclades predominately during the Late Cretaceous. These time intervals nearly coincide with periods of high precipitation (*SI Appendix*, Fig. S5) and high sea level during the Cretaceous (40, 45). Species in these habitats also exhibit pronounced phenotypic convergence (*SI Appendix*, Fig. S10 and Table S15). Moreover, the subdivision and analysis of Gerromorpha habitats remain crucial, as several species inhabit highly specialized habitats. For example, *Cavaticovelia* Andersen and Polhemus (51) and *Speovelia* Esaki (52) are restricted to lava tubes above sea level, *Lathriovelia* Andersen, 1989 occupies bamboo internodes (53), and *Oiovelia spumicola* Spangler, 1986 resides within foam masses (54). Continued research into the adaptability and evolutionary history of these specialized species is essential for advancing our understanding of the adaptive evolution of Gerromorpha.

Overall, for the water surface, its distinctive hydrodynamic constraints (18, 19, 26, 29) may allow only a single, contingent major adaptive invasion within a lineage, after which diversification and broader occupation of water-surface habitats can occur. Moreover, there is no evidence for a gradual transition through water marginal habitats; instead, colonization of the water margins results from multiple independent invasion events (Fig. 2). Although the causes of this pattern remain unclear, the complex physical conditions at the water margins, particularly the abundance of menisci at solid–liquid interfaces, are likely to be one contributing factor (27).

Constrained and Mosaic Patterns of Adaptive Expansion in Phenotypic Space during Colonizing of Water-Surface Habitats. Our results indicate that, despite some adaptive expansion and partitioning in the exploration of the phenotypic space of Gerromorpha (Fig. 2 and *SI Appendix*, Figs. S8 and S13), the overall phenotype and individual phenotypic axes—particularly those related to locomotion—demonstrate continuous, limited exploration of phenotypic space (Figs. 2 and 3 and *SI Appendix*, Fig. S14 and Table S16). There is a widespread lack of significant differences in evolutionary rates during the habitat occupation stages (*SI Appendix*, Table S21). Notably, no rapid occupation of early phenotypic space was observed, particularly during major adaptive transitions and habitat diversification. This evolutionary constraint on locomotion-related phenotypes is likely caused by the special hydrodynamic environment of water surface, which has been extensively studied (18, 19, 26–29, 55–57). Unlike terrestrial locomotion, momentum transfer during water-surface locomotion involves multiple forces exerted by the substrate, including capillary force, pressure stress, and viscous stress at the contact interface (19). The water surface must remain intact to prevent sinking (19). Hu and Bush demonstrated that among most water-surface-locomoting arthropods, capillary force plays a dominant role (19). Furthermore, according to the numerical solution for the capillary force acting on a slender cylinder on the water surface (58), the capillary force at the contact interface correlates with the wetting length, i.e., the length of the appendage in direct contact with the water surface. To support body weight and move across the water surface, while accounting for fluid resistance on wetted leg segments at different speeds and the torque balance maintained mainly by femur-tibial leverage (18, 19, 29), the body size of water striders and the relative length of their legs undergone a strongly constrained evolutionary process even during significant adaptive transitions from land to water surface (Figs. 2 and 3). Our results provide a typical case of the overall evolutionary mode of organisms inhabiting specialized interface environments, constrained by specific physical limitations.

In particular, the middle-legs segments, especially the mesotibia and mesotarsus, which directly contact the water surface and generate the main propulsive forces (22, 26, 29, 37), appear to explore a much more constrained region of phenotypic space compared to the corresponding segments of the fore- and hindlegs (Fig. 3 and *SI Appendix*, Figs. S14 and S18). In contrast, the fore- and hindleg segments—particularly the femora and tibiae, which function as levers maintaining torque balance and also perform additional biological roles [e.g., prey handling (22) and sexual conflicts (22, 59–61)]—continue to exhibit broader exploration of phenotypic space and elevated evolutionary rates (Fig. 3 and *SI Appendix*, Figs. S14 and S18). This pattern suggests a potential mechanism underlying the mosaic pattern of morphological evolution in Gerromorpha: the diversity of biological functions associated with different appendage segments directly shapes their evolutionary dynamics. Segments specialized for locomotion, such as those involved in propulsion, experience stronger environmental selection and exhibit greater evolutionary restriction, whereas segments integrating multiple ecological and behavioral functions retain

greater phenotypic lability and evolutionary potential despite similar external constraints.

More specifically, during the occupation of water-surface habitats, the mosaic pattern of phenotypic-space exploration—both in terms of positional occupation and exploratory capacity (i.e., evolutionary rate)—differs in importance between the diversification stage and the stage of stable colonization, together forming a complex adaptive landscape (Fig. 4). For instance, during the transition from terrestrial to water-surface habitats, the middle-leg segments contribute most to positional occupation, but their evolutionary rate does not correspondingly increase (Fig. 4). In contrast, antennal segments contribute more to the evolutionary rate during this transition, while contributing less to the position along the phenotypic axis (Fig. 4). These results further underscore the strong influence of biological functions on evolutionary dynamics. Meanwhile, this mosaic pattern also reflects adaptive responses to environmental differences among habitats. For example, the foreleg segments—especially the protarsus—maintains high importance in positive expansion during both the initial and stabilized stages of colonization in fast-flowing water-surface habitat (Fig. 4). This is thought to be an effective solution to counteract potential torque imbalance caused by fluid resistance on rapidly flowing torrents (29). Similarly, the consistently small body size and low evolutionary rate observed in intertidal/ocean species may represent an adaptation that facilitates hiding within coral reefs or rock crevices during high tide (22).

In summary, we demonstrate that constrained and mosaic patterns of adaptive expansion in phenotypic space are typical macroevolutionary features of colonization in water-surface habitats, which are exceptionally specialized two-phase interface environments. Using Gerromorpha, the most successful colonizing lineage in these habitats, as a model system, we show that these patterns are intricately linked to the biological functions underlying traits and to environmental differences among water-surface habitats.

Materials and Methods

Taxon Sampling. We sampled a total of 235 taxa, including 215 species from the infraorder Gerromorpha as the ingroup and 20 species from Heteroptera as outgroups, belonging to four infraorders, i.e., Dipsocoromorpha, Enicocephalomorpha, Nepomorpha, and Leptopodomorpha (Dataset S1). The ingroup includes all currently recognized family-level taxa within Gerromorpha, nearly all subfamily-level taxa (with the exception of Limnobatodinae from Hydrometridae), and approximately 56% of the genus-level taxa (data source: Integrated Taxonomic Information System, www.itis.gov). This represents the most comprehensive phylogenetic analysis of Gerromorpha to date. Three supermatrices were constructed for phylogenetic analyses: mitoPCG_123+18S28S+UCE, mitoPCG_12+18S28S+UCE, and mitoPCG_AA+18S28S+UCE (*SI Appendix*, Fig. S1). These matrices comprise sequences of 13 mitochondrial protein-coding genes (PCGs), two ribosomal DNA regions (18S and 28S rDNAs), and ultraconserved elements (UCEs) across all 235 species (Dataset S1). For the mitochondrial PCGs and rDNAs, 156 species were newly sequenced in this study, 33 species were retrieved from publicly available data on NCBI, and 45 species were obtained from transcriptomic data provided by Armisén et al. (25) (Dataset S1). For the UCE data, UCE capture experiments were conducted for 97 of these species, while UCE loci for the remaining 21 species were obtained from resequencing data, published genomes, or transcriptome data (25) (Dataset S1). All sampled taxa are deposited in GenBank, under project numbers PRJNA1415959 (62) and PRJNA1415994 (63).

Molecular Laboratory Procedures and Sequencing. Genomic DNA was extracted from thoracic muscle tissue of 192 alcohol-preserved specimens using the DNeasy Tissue Kit (Kangwei Inc.). A paired-end sequencing strategy with a 250-bp insert size and 150-bp read length was performed on the Illumina HiSeq 4000 platform at Novogene (Tianjin, China), generating 2 Gb of clean reads per individual. For UCE data, total genomic DNA was extracted using the DNeasy Blood and Tissue Kit (Qiagen, Hilden, Germany), following the manufacturer's protocols. DNA concentrations were quantified and diluted to 10 ng/μL using a Qubit fluorometer (Life Technologies, Carlsbad, CA) for library preparation. High molecular weight DNA was fragmented using the frag enzyme from the KAPA HyperPlus Kit KK8514 (Kapa Biosystems) to generate fragments ranging between 200 and 1,000 bp. Libraries were constructed following the manufacturer's protocol with minor modifications (64, 65), including half-volume reactions for all samples. Adapter-ligated products were amplified with Illumina TruSeq compatible single-indexed primers (xGen™ Stubby Adapter-UDI Primers, IDT), and KAPA Pure Beads were utilized for all cleanup steps. Libraries were pooled in equimolar amounts, resuspended in 14 μL of Tris-HCl, and enriched with the Hemiptera 2.7Kv1 UCE probes (MYbaits kit, Arbor Biosciences), which target 2,673 loci designed from ten hemipteran species, including one species of Gerromorpha (66). Enriched libraries were sequenced on the Illumina Novaseq platform at Biomarker Technologies Company (Beijing, China).

Sequence Processing and Alignment. Mitochondrial genome assembly was conducted using multiple tools, including MitoZ (67), MITObim (68), Geneious Prime 2022.2 (https://www.geneious.com), and IDBA-UD (69). Sequences of 18S and 28S rDNAs were retrieved from the assembly data using the program BLAST+. For six taxa from Chang et al. (41), stored in the NCBI SRA database, 18S and 28S rDNAs were extracted using Geneious Prime 2022.2 with reference sequences from the same subfamily. Publicly available transcriptome data were retrieved from NCBI (41), and the mitoRNA script (70) was used to extract partial mitochondrial PCGs, along with 18S and 28S rDNAs, by leveraging reference sequences from the closest related species in the dataset. This iterative approach, involving multiple rounds of data alignment and assembly, yielded high-quality results compared to direct BLAST-based methods.

The mitochondrial PCGs were initially identified using the Open Reading Frame Finder (ORF Finder, https://www.ncbi.nlm.nih.gov/orffinder/) with the invertebrate mitochondrial genetic code. Identified sequences were then compared to published mitochondrial sequences of hemipteran insects using BLAST (http://blast.ncbi.nlm.nih.gov/Blast.cgi). Gene sequences were aligned using MAFFT 7.313 (71) within PhyloSuite 1.2.2 (72), excluding stop codons. Sequences of 18S and 28S rDNAs were aligned using MAFFT 7.313 in Normal mode, and regions of questionable homology were removed using Gblocks 0.91 (73). Positions 1 and 2 of codons, as well as the amino acid sequences of PCGs, were generated using MEGA 11 (74).

Raw sequencing data of UCEs were processed using PHYLUCE v1.7.1 (75) with default values. Clean reads were assembled using SPAdes, and UCE loci were aligned with MAFFT. Internal trimming was performed using Gblocks. Data matrices were generated by excluding loci shorter than 300 bp and including loci that contained at least 50%, 55%, 60%, and 65% completeness (i.e., each single-locus alignment contained at least this percentage of the total taxa). In total, 2,714 UCE loci were recovered across 131 taxa. The final 50%, 55%, 60%, and 65% completeness data matrices comprised 129, 105, 82, and 66 loci, respectively, with total alignment lengths of 54,765 bp, 43,891 bp, 34,028 bp and 27,977 bp. Further details of the concatenated matrices are provided in *SI Appendix*, Table S3. Based on a comprehensive evaluation balancing locus number, alignment length, and data completeness, the 60% completeness matrix (82 loci; 34,028 bp) was selected for all subsequent analyses.

Individual genes were then concatenated to generate the following datasets: mitoPCG_123+18S28S+UCE (51,380 aligned sites, including all three codon positions of the mitochondrial PCGs, 18S rDNA, 28S rDNA, and UCE loci), mitoPCG_12+18S28S+UCE (47,668 aligned sites, including codon positions 1 and 2 of the mitochondrial PCGs, 18S rDNA, 28S rDNA, and UCE loci), and mitoPCG_AA+18S28S+UCE (44,279 aligned sites, including amino acid sequences of the mitochondrial PCGs, 18S rDNA, 28S rDNA, and UCE loci).

Substitution Saturation and Heterogeneity Tests. To evaluate substitution saturation in the dataset mitoPCG_123, the software DAMBE 7.2.43 (76) was utilized. Given the limitation of DAMBE, which can process a maximum of 32 taxa at a time, the dataset comprising taxa was randomly divided into nine groups for analyses. The heterogeneity of sequence composition within the dataset was assessed using AliGROOVE (77), with all parameters set to their default values, except for the treatment of indels, which were considered ambiguous characters.

Phylogenetic Analyses. For each dataset partition (i.e., mitoPCG_123+18S28S+UCE, mitoPCG_12+18S28S+UCE, and mitoPCG_AA+18S28S+UCE), ModelFinder (78), and PartitionFinder 2 (79) were employed to identify the optimal partitioning strategies and substitution models, guided by the Bayesian Information Criterion (BIC) (*SI Appendix*, Table S2). Phylogenetic relationships were inferred using IQ-TREE2 (80) through maximum likelihood (ML) analyses, applying the best-fit partitioned models while adhering to topological constraints at the genus level derived from the transcriptome-based phylogeny of Armisén et al. (25). To accommodate compositional heterogeneity, the datasets mitoPCG_123+18S28S+UCE and mitoPCG_12+18S28S+UCE were also evaluated under the GHOST model (-MFP+GHOST) while maintaining the same topological backbone (81). All ML analyses included assessments of nodal support, incorporating 1,000 SH-aLRT replicates and 1,000 ultrafast bootstrap iterations. Additionally, CAT-model analyses (CAT-GTR and CAT-POISSON) were implemented in PhyloBayes MPI 1.8b (82) using the respective IQ-TREE GHOST topologies as guide trees. Each analysis involved two independent Markov Chain Monte Carlo (MCMC) chains, with convergence monitored via bpcomp (maxdiff < 0.3) and tracecomp (ESS > 50). After discarding the initial 10% of each chain as burn-in, consensus trees and posterior probabilities (PP) were calculated from the combined post-burn-in trees of both runs. The species tree was reconstructed using ASTRAL-III (83) within a coalescent framework. For the mitoPCG_123+18S28S+UCE dataset, gene trees were initially inferred for each locus through ML analyses in IQ-TREE with ModelFinder (MFP) optimization, followed by summarization into a species tree using ASTRAL-III with default settings.

Divergence Time Estimation. For divergence time estimation, we selected the ML results derived from the concatenated mitoPCG_123+18S28S+UCE (MFP+GHOST) dataset, considering factors such as the data matrix size, the number of species, supporting values for key lineages, and inclusion of critical taxa. Seventeen fossils were integrated into the analysis, establishing 12 calibration points throughout the phylogenetic tree (*SI Appendix*, Table S4). Divergence times were estimated using MCMCTREE in PAML v4.9i (84) (*SI Appendix*, Fig. S1), employing the approximate likelihood method to enhance computational efficiency (85). The time unit was set to 100 Ma, with a hard maximum bound for the root set at 314 Ma, reflecting the age of the oldest known fossil of Hemiptera (86). The ML estimates of branch lengths, gradient vectors, and Hessian matrices were calculated using the GTR+G substitution model (model = 7). The overall substitution rate (rgene_gamma) and rate-drift parameter (sigma2_gamma) were set to 2, 20, 1 and 1, 10, 1, respectively. Two independent MCMC runs were executed, discarding the first 1,000,000 iterations as burn-in, and sampling continued at 100-iteration intervals until a total of 50,000 samples was achieved. Convergence of the MCMC analyses was assessed using Tracer 1.7 (87), ensuring that all parameter ESS values exceeded the threshold of 200.

We also utilized r8s 1.8.1 (88) to assess the robustness of the divergence time estimated by MCMCTREE (*SI Appendix*, Fig. S1). The ML tree derived from the mitoPCG_123+18S28S+UCE (MFP+GHOST) dataset, including branch length information, was used as a fixed input tree for divergence time estimation. The cross-validation method in r8s was applied to identify the optimal smoothing level for penalized likelihood analyses, with smoothing parameters ranging from 1 to 1,000. To estimate 95% CI for divergence times, 100 bootstrap datasets were generated from the mitoPCG_123+18S28S+UCE dataset using SEQBOOT from PHYLIP 3.6 (89), and branch lengths for each bootstrapped dataset were subsequently estimated using PAUP 4.0 (90).

Evolutionary Reconstructions of Habitats Occupation History. Gerromorphan taxa occupy a wide range of aquatic habitats, from small, isolated water bodies to expansive oceanic surfaces; some species also inhabit humid terrestrial environments (22). Here, we identified eight typical habitat types for Gerromorpha, following Andersen's (22) habitat classification: A) Humid terrestrial habitats, (moist banks near freshwater and damp leaf litter); B) Marginal areas of freshwater (the narrow water-surface area at the land–water interface, characterized by emergent plants or floating leaves), where insects often must navigate complex transitions between solid substrates and the liquid surface; C) Hygropetric habitats (rocks or cliffs covered by a thin film of freshwater, typically near vertical); D) Open, stagnant freshwater surfaces (open areas of stagnant lakes, away from the land, where the primary survival pressure arises from traversing long distances on the water surface in search of food (22); E) Fast-flowing freshwater surfaces (the central regions of large rivers or streams, where inhabitants typically experience significant water-flow resistance); F) Slow-flowing freshwater surfaces (small springs or nearly quiet parts of streams, which represent the typical habitat for most Gerromorpha); G) Intertidal sandy and rocky areas (coastal terrestrial habitats occupied by a limited number of specialized species); H) Intertidal areas (brackish water regions, such as estuaries and mangroves) and ocean surfaces, where insects colonizing these areas must contend with tidal fluctuations; during high tide, they often conceal themselves in the crevices of rocks.

Using field observations and literature data, we assigned habitat states for the sampled species to these categories (Datasets S1 and S2). Although some taxa exhibit multiple habitat preferences, we restricted each taxon's habitat classification to its optimal or most dominant habitat. To analyze the evolutionary patterns of occupation of habitats, we estimated transition rates and ancestral states using the Markov model within three parameterizations of transition rates (equal rates, ER; symmetrical, SYM; and all rates different, ARD) with two or without "hidden" states for each observable state using *corHMM* function in R package *corHMM* v2.8 (91) (*SI Appendix*, Fig. S1). The model with the lowest delta AICc value was selected as the best-fit model. The state of each internal node with the highest probability of habitat occupancy and habitat transition rate categories based on reconstruction results from the best-fit model was extracted for subsequent analyses.

Macroevolutionary Analyses of Phenotypic Traits and Diversification Rates Analyses.

Diversification rates analyses. We obtained the number of known gerromorphan species from the Integrated Taxonomic Information System (ITIS; https://itis.gov/) as of September 2, 2024. Diversification rate analyses were conducted using the speciation/extinction model implemented in BAMM (92). To account for incomplete and biased taxon sampling, as well as the paraphyletic relationships among subfamilies within Gerromorpha, appropriate sampling fractions were assigned to all major monophyletic clades in the phylogenetic dataset (*SI Appendix*, Table S7). Prior values, i.e., the initial lambda, the lambda shift parameter, and the extinction rate, were determined using the *setBAMMpriors* function in the R package *BAMMtools* (*SI Appendix*, Table S8). Four independent Markov chain Monte Carlo (MCMC) simulations were run for a minimum of 20,000,000 generations, with Bayesian inference performed using the Metropolis-coupled MCMC algorithm. The initial 10% of samples from each chain were discarded as burn-in. Convergence was assessed by confirming that the ESS for both the number of rate shifts and the log-likelihood exceeded 200. Shift configuration data were extracted using the *getEventData* function, and the results were visualized accordingly.

Morphological data collection. Given the critical role of leg length in surface locomotion and adaptability of water striders (22, 25, 37), as well as the availability of literature data and specimens, we focused on collecting measurements of appendage lengths and body length. We compiled 14 continuous phenotypic traits from 186 gerromorphan species (784 samples in total) using direct measurements and information from primary taxonomic literature (Dataset S1 and *SI Appendix*, Fig. S1). These traits included the lengths of various segments of the legs and antennae. Among these traits, only the total tarsal length was considered instead of measuring each individual segment, due to the complex fusion of tarsal segments observed across different lineages (22). Each trait was measured from three individual samples of each sex, and the measurements were averaged. For species with limited availability of specimens or data, single values or interval medians reported in the literature were used. In cases where literature data or specimens were unavailable for specific species, the missing phenotypic data were substituted using measurements from closely related congeneric species (Dataset S1). To standardize the data, the ratio of each phenotypic measurement to body length was calculated as the relative length, body length, and all relative lengths were log-transformed using the natural logarithm. We also extracted all available measurement data for 59 extinct gerromorphan species from the literature (Dataset S1).

The discrete phenotypic dataset was derived from the morphological data matrix previously developed by Damgaard (36) for all gerromorphan families and subfamilies (Datasets S1 and S2), and the locomotion types of gerromorphans were coded based on natural observations (Datasets S1 and S2). This dataset included microstructural traits of the body, as well as morphological

characters associated with the head, thorax, abdomen, and eggs. Characters that overlapped or were directly associated with the measured traits were excluded. In total, 54 discrete phenotypic characters were collected and mapped across all sampled species.

Occupation and partitioning patterns of phenotype space analyses. Principal component analysis (PCA), phylogenetic PCA (pPCA) and phylogenetically aligned component analysis (PaCA) were conducted to characterize the occupation patterns of phenotypic space regarding the relative length of appendages in Gerromorpha, utilizing all log-transformed relative measurements (excluding body length). The analyses were performed with the *gm.prcomp* function in the R package *geomorph* v4.0.10 (93), using the time-calibrated ultrametric tree obtained above (*SI Appendix*, Fig. S1). Considering the proportions of variance and cumulative proportions of variance explained by the principal component axes for each analysis (*SI Appendix*, Table S10), we selected the results derived from PaCA to represent overall phenotypic variation.

The PC1 values derived from PaCA and the original variable coordinates of ancestral nodes were reconstructed based on the BM model using *fastAnc* function in the R package *phytools* version 2.4-4 (94) and the evolutionary trajectories were plotted using the *phenogram* function. Considering the limited fossil data and the presence of temporal distribution bias, we used a 5-Mya sliding window to assess the differences between fossil data and the reconstructed results for each phenotypic axis within each window using the Wilcoxon sum-rank test. Besides, the highest probability states of habitat occupancy and habitat transition rate categories were mapped onto the corresponding ancestral nodes. Wilcoxon rank-sum tests were performed to compare the coordinates of each phenotypic axis across different habitat occupancy states. The coordinates of ancestral nodes in the principal component space were mapped through a linear transformation.

To investigate patterns of phenotypic-space partitioning, we used the *hypervolume* function from the R package *hypervolume* version 3.1.6 (95) with a Gaussian kernel to calculate hypervolume occupancy within the phenotypic space, based on the first two principal components (PC1 and PC2) derived from the PaCA results. For pairwise comparisons between extant species in different habitats and between different states in habitat-occupancy history, we calculated hypervolume overlap for all pairs using the Jaccard similarity index and Sørensen similarity index, as well as the unique fraction, centroid distances between hypervolumes, and minimum distances.

Convergent evolution assessment. We used the *calcConvCt* function from the R package *convevol* version 2.2.1 (96) to calculate C1–C4 indices, which quantify the strength of phenotypic convergence within different habitats for overall phenotypic variation (PC1 values derived from the PaCA results) as well as for each individual phenotypic axis. The C1–C4 indices are based on the ratio of the current distance between two lineages in morphospace (Dtip) to the maximum reconstructed distance between the two lineages at any point in the past (Dmax) (97). Given that the number of synchronous nodes within each habitat was nearly zero, we did not use the recently developed Ct1–Ct4 indices. We applied *convSig* function to obtain the distribution from 100 simulations and to assess the significance of convergence strength. *P*-values for each C index under different habitat classifications within each phenotypic axis were adjusted using the Benjamini–Hochberg (BH) procedure.

Spatial exploration dynamics of overall phenotypic variation and along each phenotypic axis. To evaluate the spatial exploration disparity dynamics of Gerromorpha species in overall phenotypic space and along individual phenotypic axes, the *dtt* function from the R package *geiger* version 2.0.11 (98) was used to explore the patterns of empirical disparity and mean expectational disparity through time under a BM model for overall phenotypic variation (PC1 values derived from PaCA) and individual phenotypic axis values (including log-transformed body length). The global morphological disparity indexes (MDI) were calculated to evaluate the overall difference between empirical disparity and mean expectational disparity, significances were evaluated via the MDI *P*-values comparing the empirical value with 1,000 simulations. To investigate the dynamics of MDI over time, we constructed an interpolation function for the temporal values of MDI, segmenting the time axis into 20 slices, and computed overall phenotypic variance and integrated MDI value along each phenotypic axis within each time slice.

Phenotypic evolutionary rates analyses. For each continuous axis, we employed a phenotypic evolution model implemented in BAMM (92). The extended BAMM framework enables the modeling of time-dependent phenotypic evolution and macroevolutionary rate heterogeneity (99) and has been applied in various studies of phenotypic macroevolution (99, 100). In this model, the parameter "beta" represents the instantaneous rate of phenotypic evolution at any given time. Prior values were determined using the *setBAMMpriors* function in the R package *BAMMtools* (*SI Appendix*, Table S8). The SD of the rate-change parameters was fixed as a constant. A uniform prior density was applied to the ancestral character states, with bounds determined by the minimum and maximum observed data. Other model parameters were kept at their default settings. Four Markov Chain Monte Carlo (MCMC) were run for at least 500,000 generations, and Bayesian inference was conducted using Metropolis-coupled MCMC. The first 10% of samples were discarded as burn-in. Convergence was assessed by ensuring that the ESS for the number of rate shifts and the log-likelihood values exceeded 200. Shift configuration data were analyzed using the *getEventData* function, and the results were visualized accordingly. Evolutionary rates of tips and internal nodes were extracted (where the evolutionary rate of an internal node is the average evolutionary rate of the edge represented by its parent node) for subsequent analyses.

The importance of phenotypic axes and phenotypic evolution rates in habitat colonization history. We extracted the reconstructed trait values and corresponding evolutionary rates for each phenotypic axis at all ancestral nodes on the time-calibrated tree, and mapped these data to the habitat occupancy history. Some habitats exhibited insufficient data points; for instance, "Hygropetric habitats" and "Intertidal sandy and rocky areas" were excluded in the analyses. Subsequently, we constructed random-forest models using the R package *randomForest* version 4.7-1.2 (101), employing the reconstructed phenotypic values and the phenotypic evolutionary rates of each ancestral node as independent variables, with habitat type or habitat occupancy status as classification labels. Each model was trained using 2,000 decision trees (ntree = 2,000). The predictive performance of the models reflects the overall information content of different phenotypic traits in distinguishing among habitat categories. We quantified the relative importance of each phenotypic axis in the models using the Mean Decrease in Accuracy (MDA) metric, a larger value indicating a greater weight or contribution of that phenotypic axis to the classification. To assess the significance of the importance metric, we randomly shuffled the classification labels 2,000 times, retrained the random-forest model under each permutation, and recorded the MDA value for each phenotypic axis, thereby constructing a random null distribution of variable importance. We then compared the MDA of the real model with this random distribution to estimate the *P*-value, determining whether the importance of each phenotypic axis was significantly greater than random. Wilcoxon rank-sum tests were performed to compare values and evolutionary rates of different phenotypic axes across various habitat occupancy stages.

Correlation analyses between phenotypic evolution rates and net diversification rate. To assess the impact of phenotypic evolution rates along each phenotypic axis on net diversification rates, while considering habitat differences during different periods of habitat occupancy, we employed bootstrap resampling analysis based on LASSO regression (Least Absolute Shrinkage and Selection Operator). First, using the phenotypic evolution rate matrix and habitat occupancy history matrix obtained as described above, along with the net diversification rate of ancestral nodes, we performed LASSO regression modeling within different groups, treating net diversification rate as the response variable and the phenotypic evolution rates of each phenotypic axis as predictor variables. LASSO regression implements variable selection through a penalty term, which shrinks some coefficients to 0, thereby identifying the features that most strongly influence rate changes. To evaluate the robustness of the model results, we conducted 100 Bootstrap resamplings. In each iteration, samples were randomly drawn with replacement, and the penalty parameter λ was automatically determined based on cross-validation using the R package *glmnet* version 4.1-10 (102). Model coefficients were extracted at the *lambda.1se* level to obtain more robust results. The regression coefficients of each model were stored in a repetition matrix, constructing the parameter distribution under different sampling scenarios. Subsequently, we calculated the average regression coefficient and SD of each phenotypic axis across the 100 resamplings. The average coefficient reflects the overall influence direction and effect intensity on the net speciation rate. By comparing the mean coefficient values, we identified key phenotypic features that significantly influence changes in the net diversification rate among different habitats during different stages of habitat occupancy.

Ancestral state reconstruction of discrete traits. For the 54 discrete characters, we continued to use the *corHMM* function to perform maximum likelihood

estimation and to compare models with and without hidden states based on three parameterizations of transition rates, following the same procedure as the habitat data analyses described above. We selected the best-fit model and its reconstruction results using delta AICc as the criterion. We defined the comparison between the tip state of each discrete phenotype and the reconstructed root state as the net evolutionary change: for each discrete phenotype, the net change is 0 if it matches the root state and 1 if it differs. We then tabulated the distribution of net evolutionary changes for discrete traits among species occupying different habitats. Model selection and reconstruction for movement modes were carried out as described above.

Data, Materials, and Software Availability. DNA sequencing data generated in this study have been deposited in the NCBI Sequence Read Archive (SRA) under BioProject accession numbers PRJNA1415994 (63) and PRJNA1415959 (62). Details of the DNA sequencing datasets downloaded from NCBI Datasets are provided in Dataset S1. The habitats dataset (species analyzed in this study), the continuous dataset (extant species analyzed in this study and fossil species), and the discrete dataset (species analyzed in this study) are also available in Dataset S1. All other data are included in the manuscript and/or supporting information.

ACKNOWLEDGMENTS. We thank Zuqi Mai, Xin Xie, Danyang Zhou, Zehao Ma, Chao Wu and Fan Gao for providing habitats' photographs. This study was supported by National Natural Science Foundation of China (No. 32322012, 32470467, 32130014).

Author affiliations: [a]Institute of Entomology, College of Life Sciences, Nankai University, Tianjin 300071, China; [b]Laboratory of Entomology, Wageningen University and Research, Wageningen 6700 AA, The Netherlands; [c]Institute of Environment, Florida International University, Miami, FL 33181; [d]Natural History Museum of Denmark, Zoological Museum, Copenhagen Ø 2100, Denmark; [e]Institute of Infection, Veterinary and Ecological Sciences, University of Liverpool, Liverpool, Merseyside L3 5RF, United Kingdom; [f]Laboratorio de Entomología, Instituto de Biodiversidad y Biología Experimental y Aplicada, Consejo Nacional de Investigaciones Científicas y Técnicas - Universidad de Buenos Aires, Departamento de Biodiversidad y Biología Experimental - Facultad de Ciencias Exactas y Naturales, Universidad de Buenos Aires, Buenos Aires C1428EHA, Argentina; [g]Department of Biology, Faculty of Chemistry, Biology, Geography, West University of Timişoara, Timişoara 300115, Romania; [h]Research Institute on Terrestrial Ecosystems, National Research Council of Italy, Sesto Fiorentino (Florence) I-50019, Italy; [i]"La Specola" Museum, Natural History Museum, University of Florence, Florence I-50125, Italy; [j]Department of Natural Sciences, Bishop Museum, Honolulu, HI 96734; [k]Ishikawa Insect Museum, Hakusan, Ishikawa 920–2113, Japan; [l]Fukuoka Institute of Health and Environmental Sciences, Dazaifu, Fukuoka 818−0135, Japan; [m]Laboratory for Emerging Infectious Diseases, Faculty of Science, University of Buea, Buea PO Box 63, Cameroon; and [n]School of Bioengineering, Qilu University of Technology (Shandong Academy of Sciences), Jinan, Shandong 250353, China

Author contributions: W.B. and Z.Y. designed research; Z.J., M.Q., S.F., Z. Li, and B.G. performed research; Z.J., M.Q., B.G., H.L., Z. Leng, C.L., B.Z., and H.Y. analyzed data; Z.J., M.Q., S.F., Z. Li, H.L., Z. Leng, M.R.P., J.D., B.L.M., S.A.M., G.M.B., F.C., D.A.P., K.W., J.N., S.E., C.L., B.Z., H.Y., S.W., H.X., and Z.Y. contributed material collection; and Z.J., M.Q., and Z.Y. wrote the paper.

1. G. G. Simpson, *The Major Features of Evolution* (Columbia University Press, 1953).
2. D. Schluter, *The Ecology of Adaptive Radiation* (OUP Oxford, 2000).
3. J. B. Yoder *et al.*, Ecological opportunity and the origin of adaptive radiations. *J. Evol. Biol.* **23**, 1581–1596 (2010).
4. A. H. Miller *et al.*, The ecology and evolution of key innovations. *Trends Ecol. Evol.* **38**, 122–131 (2023).
5. G. Navalón *et al.*, Environmental signal in the evolutionary diversification of bird skeletons. *Nature* **611**, 306–311 (2022).
6. P. O. Title *et al.*, The macroevolutionary singularity of snakes. *Science* **383**, 918–923 (2024).
7. A. Orkney *et al.*, Evolutionary integration of forelimb and hindlimb proportions within the bat wing membrane inhibits ecological adaptation. *Nat. Ecol. Evol.* **9**, 111–123 (2025).
8. F. Alfieri *et al.*, A macroevolutionary common-garden experiment reveals differentially evolvable bone organization levels in slow arboreal mammals. *Commun. Biol.* **6**, 995 (2023).
9. C. J. Law *et al.*, Uncovering the mosaic evolution of the carnivoran skeletal system. *Biol. Lett.* **20**, 20230526 (2024).
10. E. J. Coombs *et al.*, The tempo of cetacean cranial evolution. *Curr. Biol.* **32**, 2233–2247 (2022).
11. T. R. Simões, S. E. Pierce, Sustained high rates of morphological evolution during the rise of tetrapods. *Nat. Ecol. Evol.* **5**, 1403–1414 (2021).
12. J. R. G. Rawson *et al.*, Early tetrapod cranial evolution is characterized by increased complexity, constraint, and an offset from fin-limb evolution. *Sci. Adv.* **8**, eadc8875 (2022).
13. N. P. Kelley, N. D. Pyenson, Evolutionary innovation and ecology in marine tetrapods from the Triassic to the Anthropocene. *Science* **348**, aaa3716 (2015).
14. Y. Yu *et al.*, Complex macroevolution of pterosaurs. *Curr. Biol.* **33**, 770–779 (2023).
15. T. A. Dececchi, H. C. E. Larsson, Body and limb size dissociation at the origin of birds: Uncoupling allometric constraints across a macroevolutionary transition. *Evolution* **67**, 2741–2752 (2013).
16. K. M. Evans *et al.*, Integration drives rapid phenotypic evolution in flatfishes. *Proc. Natl. Acad. Sci. U.S.A.* **118**, e2101330118 (2021).
17. F. A. López-Romero *et al.*, Evolution of the Batoidea pectoral fin skeleton: Convergence, modularity, and integration driving disparity trends. *Evol. Ecol.* **39**, 111–134 (2025).
18. J. W. Bush *et al.*, The integument of water-walking arthropods: Form and function. *Adv. Insect Physiol.* **34**, 117–192 (2007).
19. D. L. Hu, J. W. Bush, The hydrodynamics of water-walking arthropods. *J. Fluid Mech.* **644**, 5–33 (2010).
20. J. W. Glasheen, T. A. McMahon, A hydrodynamic model of locomotion in the basilisk lizard. *Nature* **380**, 340–342 (1996).
21. S. T. Hsieh, G. V. Lauder, Running on water: Three-dimensional force generation by basilisk lizards. *Proc. Natl. Acad. Sci. U.S.A.* **101**, 16784–16788 (2004).
22. N. M. Andersen, *The Semiaquatic Bugs* (Scandinavian Science Press, 1982).
23. J. T. Polhemus, D. A. Polhemus, Global diversity of true bugs (Heteroptera; Insecta) in freshwater. *Hydrobiologia* **595**, 379–391 (2008).
24. P. Chen *et al.*, *The Aquatic and Semi-Aquatic Bugs (Heteroptera: Nepomorpha & Gerromorpha) of Malesia* (Brill N.V. Press, 2005).
25. D. Armisén *et al.*, Transcriptome-based phylogeny of the semi-aquatic bugs (Hemiptera: Heteroptera: Gerromorpha) reveals patterns of lineage expansion in a series of new adaptive zones. *Mol. Biol. Evol.* **39**, msac229 (2022).
26. D. L. Hu *et al.*, The hydrodynamics of water strider locomotion. *Nature* **424**, 663–666 (2003).
27. D. L. Hu, J. W. Bush, Meniscus-climbing insects. *Nature* **437**, 733–736 (2005).
28. X. Gao, L. Jiang, Water-repellent legs of water striders. *Nature* **432**, 36 (2004).
29. W. Kim *et al.*, Physics of sliding on water explains morphological and behavioural allometry across a wide range of body sizes in water striders (Gerridae). *Proc. R. Soc. B* **291**, 20241357 (2024).
30. M. E. Santos *et al.*, Taxon-restricted genes at the origin of a novel trait allowing access to a new environment. *Science* **358**, 386–390 (2017).
31. A. Khila *et al.*, Evolution of a novel appendage ground plan in water striders is driven by changes in the Hox gene Ultrabithorax. *PLoS Genet.* **5**, e1000583 (2009).
32. A. Khila *et al.*, Comparative functional analyses of ultrabithorax reveal multiple steps and paths to diversification of legs in the adaptive radiation of semi-aquatic insects. *Evolution* **68**, 2159–2170 (2014).
33. D. Armisén *et al.*, Predator strike shapes antipredator phenotype through new genetic interactions in water striders. *Nat. Commun.* **6**, 8153 (2015).
34. P. N. Refki *et al.*, Emergence of tissue sensitivity to Hox protein levels underlies the evolution of an adaptive morphological trait. *Dev. Biol.* **392**, 441–453 (2014).
35. P. N. Refki, A. Khila, Key patterning genes contribute to leg elongation in water striders. *Evodevo* **6**, 14 (2015).
36. J. Damgaard, Phylogeny of the semiaquatic bugs (Hemiptera-Heteroptera, Gerromorpha). *Insect Syst. Evol.* **39**, 431–460 (2008).
37. A. J. J. Crumière *et al.*, Diversity in morphology and locomotory behavior is associated with niche expansion in the semi-aquatic bugs. *Curr. Biol.* **26**, 3336–3342 (2016).
38. Y. Wang *et al.*, Diversification of true water bugs revealed by transcriptome-based phylogenomics. *Syst. Entomol.* **46**, 339–356 (2021).
39. Y. Wang *et al.*, 300 million years of coral treaders (Insecta: Heteroptera: Hermatobatidae) back to the ocean in the phylogenetic context of Arthropoda. *Proc. R. Soc. B* **290**, 20230855 (2023).
40. Z. Ye *et al.*, Phylogenomic reconstruction illuminates the evolutionary history of freshwater to marine transition in the subfamily Haloveliinae (Hemiptera: Heteroptera: Veliidae). *Syst. Entomol.* **49**, 330–343 (2024).
41. J. J. M. Chang *et al.*, Skimming the skaters: Genome skimming improves phylogenetic resolution of Halobatinae (Hemiptera: Gerridae). *Insect Syst. Divers.* **8**, 3 (2024).
42. M. J. Raupach *et al.*, Exploring the phylogenetic history of water striders (Hemiptera: Heteroptera: Gerromorpha) using genome-skimming. *Syst. Entomol.* **51**, e70022 (2026).
43. A. Hallam, A review of mesozoic climates. *J. Geol. Soc.* **142**, 433–445 (1985).
44. M. Holz, Mesozoic paleogeography and paleoclimates–A discussion of the diverse greenhouse and hothouse conditions of an alien world. *J. South Am. Earth Sci.* **61**, 91–107 (2015).
45. A. C. Chaboureau *et al.*, Tectonic-driven climate change and the diversification of angiosperms. *Proc. Natl. Acad. Sci. U.S.A.* **111**, 14066–14070 (2014).
46. Y. Donnadieu *et al.*, A GEOCLIM simulation of climatic and biogeochemical consequences of Pangea breakup. *Geochem. Geophys. Geosyst.* **7**, Q11019 (2006).
47. B. Wang *et al.*, Ecological radiations of insects in the mesozoic. *Trends Ecol. Evol.* **37**, 529–540 (2022).
48. J. Damgaard, Evolution of the semi-aquatic bugs (Hemiptera: Heteroptera: Gerromorpha) with a re-interpretation of the fossil record. *Acta Entomol. Mus. Natl. Pragae* **48**, 251–268 (2008).
49. K. P. Johnson *et al.*, Phylogenomics and the evolution of hemipteroid insects. *Proc. Natl. Acad. Sci. U.S.A.* **115**, 12775–12780 (2018).
50. V. Perrichot *et al.*, Gerromorphan bugs in early Cretaceous French amber (Insecta: Heteroptera): First representatives of Gerridae and their phylogenetic and palaeoecological implications. *Cretac. Res.* **26**, 793–800 (2005).
51. N. M. Andersen, J. T. Polhemus, Four new genera of Mesoveliidae (Hemiptera, Gerromorpha) and the phylogeny and classification of the family. *Entomol. Scand.* **11**, 369–392 (1980).
52. T. Esaki, A remarkable speo-halophilous water strider (Heteroptera, Mesoveliidae). *Ann. Mag. Nat. Hist. Ser.* **4**, 341–346 (1929).
53. D. Kovac, C. M. Yang, Revision of the Oriental bamboo-inhabiting semiaquatic bugs genus *Lathriovelia* Andersen, 1989 (Heteroptera: Velidae) with description of *L. rickmersi*, new species and notes on the genus *Baptista* Distant, 1903. *Raffles Bull. Zool.* **48**, 153–165 (2000).
54. P. J. Spangler, Two new species of water striders of the genus *Oiovelia* from the Tepui Cerro de la Neblina, Venezuela (Hemiptera: Veliidae). *Proc. Entomol. Soc. Wash.* **88**, 438–450 (1986).
55. J. S. Koh, Jumping on water: Surface tension–dominated jumping of water striders and robotic insects. *Science* **349**, 517–521 (2015).
56. P. Gao, J. J. Feng, A numerical investigation of the propulsion of water walkers. *J. Fluid Mech.* **668**, 363–383 (2011).
57. T. Steinmann *et al.*, Singularity of the water strider propulsion mechanisms. *J. Fluid Mech.* **915**, A118 (2021).
58. D. Vella, Floating objects with finite resistance to bending. *Langmuir* **24**, 8701–8706 (2008).
59. L. Rowe *et al.*, Functional significance of elaborate secondary sexual traits and their evolution in the water strider genus *Rheumatobates*. *Can. Entomol.* **138**, 568–577 (2006).
60. A. J. J. Crumière *et al.*, Escalation and constraints of antagonistic armaments in water striders. *Front. Ecol. Evol.* **7**, 215 (2019).

61. A. J. J. Crumière, A. Khila, Hox genes mediate the escalation of sexually antagonistic traits in water striders. *Biol. Lett.* **15**, 20180720 (2019).
62. Z. Jin, M. Qiao, Gerromorpha sequencing for mitochondrial and UCE part 1. Sequence Read Archive. https://www.ncbi.nlm.nih.gov/sra/PRJNA1415959. Deposited 22 February 2026.
63. Z. Jin, M. Qiao, Gerromorpha sequencing for mitochondrial part 2. Sequence Read Archive. https://www.ncbi.nlm.nih.gov/sra/PRJNA1415994. Deposited 22 February 2026.
64. M. Forthman *et al.*, Phylogenomic analysis suggests Coreidae and Alydidae (Hemiptera: Heteroptera) are not monophyletic. *Zool. Scr.* **48**, 520–534 (2019).
65. T. J. Kieran *et al.*, Insight from an ultraconserved element bait set designed for hemipteran phylogenetics integrated with genomic resources. *Mol. Phylogenet. Evol.* **130**, 297–303 (2019).
66. B. C. Faircloth, Identifying conserved genomic elements and designing universal bait sets to enrich them. *Methods Ecol. Evol.* **8**, 1103–1112 (2017).
67. G. Meng *et al.*, MitoZ: A toolkit for animal mitochondrial genome assembly, annotation and visualization. *Nucleic Acids Res.* **47**, e63 (2019).
68. C. Hahn *et al.*, Reconstructing mitochondrial genomes directly from genomic next-generation sequencing reads–a baiting and iterative mapping approach. *Nucleic Acids Res.* **41**, e129 (2013).
69. Y. Peng *et al.*, IDBA-UD: A de novo assembler for single-cell and metagenomic sequencing data with highly uneven depth. *Bioinformatics* **28**, 1420–1428 (2012).
70. G. Forni *et al.*, Complete mitochondrial genomes from transcriptomes: Assessing pros and cons of data mining for assembling new mitogenomes. *Sci. Rep.* **9**, 14806 (2019).
71. K. Katoh, D. M. Standley, MAFFT multiple sequence alignment software version 7: Improvements in performance and usability. *Mol. Biol. Evol.* **30**, 772–780 (2013).
72. D. Zhang *et al.*, PhyloSuite: An integrated and scalable desktop platform for streamlined molecular sequence data management and evolutionary phylogenetics studies. *Mol. Ecol. Resour.* **20**, 348–355 (2020).
73. G. Talavera, J. Castresana, Improvement of phylogenies after removing divergent and ambiguously aligned blocks from protein sequence alignments. *Syst. Biol.* **56**, 564–577 (2007).
74. K. Tamura *et al.*, MEGA11: Molecular evolutionary genetics analysis version 11. *Mol. Biol. Evol.* **38**, 3022–3027 (2021).
75. B. C. Faircloth, PHYLUCE is a software package for the analysis of conserved genomic loci. *Bioinformatics* **32**, 786–788 (2016).
76. X. Xia, DAMBE7: New and improved tools for data analysis in molecular biology and evolution. *Mol. Biol. Evol.* **35**, 1550–1552 (2018).
77. P. Kück *et al.*, AliGROOVE–Visualization of heterogeneous sequence divergence within multiple sequence alignments and detection of inflated branch support. *BMC Bioinformatics* **15**, 294 (2014).
78. S. Kalyaanamoorthy *et al.*, ModelFinder: Fast model selection for accurate phylogenetic estimates. *Nat. Methods* **14**, 587–589 (2017).
79. R. Lanfear *et al.*, PartitionFinder 2: New methods for selecting partitioned models of evolution for molecular and morphological phylogenetic analyses. *Mol. Biol. Evol.* **34**, 772–773 (2016).
80. B. Q. Minh *et al.*, IQ-TREE 2: New models and efficient methods for phylogenetic inference in the genomic era. *Mol. Biol. Evol.* **37**, 1530–1534 (2020).
81. S. M. Crotty *et al.*, GHOST: Recovering historical signal from heterotachously evolved sequence alignments. *Syst. Biol.* **69**, 249–264 (2020).
82. N. Lartillot *et al.*, PhyloBayes MPI: Phylogenetic reconstruction with infinite mixtures of profiles in a parallel environment. *Syst. Biol.* **62**, 611–615 (2013).
83. C. Zhang *et al.*, ASTRAL-III: Polynomial time species tree reconstruction from partially resolved gene trees. *BMC Bioinformatics* **19**, 153 (2018).
84. Z. Yang, PAML 4: Phylogenetic analysis by maximum likelihood. *Mol. Biol. Evol.* **24**, 1586–1591 (2007).
85. M. dos Reis, Z. Yang, Approximate likelihood calculation on a phylogeny for Bayesian estimation of divergence times. *Mol. Biol. Evol.* **28**, 2161–2172 (2011).
86. A. Nel *et al.*, The earliest known holometabolous insects. *Nature* **503**, 257–261 (2013).
87. A. Rambaut *et al.*, Posterior summarization in Bayesian phylogenetics using Tracer 1.7. *Syst. Biol.* **67**, 901–904 (2018).
88. M. J. Sanderson, r8s: Inferring absolute rates of molecular evolution and divergence times in the absence of a molecular clock. *Bioinformatics* **19**, 301–302 (2003).
89. J. Felsenstein, PHYLIP (Phylogeny Inference Package) (Version 3.66, Genomes Sciences, Department of Genetics, Distributed by Author, Department of Genome Sciences, University of Washington, Seattle, WA, 2006).
90. J. C. Wilgenbusch, D. Swofford, Inferring evolutionary trees with PAUP*. *Curr. Protoc. Bioinformatics* **6**, Unit 6.4 (2003).
91. J. Beaulieu *et al.*, corHMM: Hidden Markov Models of Character Evolution (2022). https://cran.r-project.org/package=corHMM. Accessed 26 October 2025.
92. D. L. Rabosky *et al.*, Rates of speciation and morphological evolution are correlated across the largest vertebrate radiation. *Nat. Commun.* **4**, 1958 (2013).
93. E. Baken *et al.*, geomorph v4.0 and gmShiny: Enhanced analytics and a new graphical interface for a comprehensive morphometric experience. *Methods Ecol. Evol.* **12**, 2355–2363 (2021).
94. L. J. Revell, Phytools: An R package for phylogenetic comparative biology (and other things). *Methods Ecol. Evol.* **3**, 217–223 (2012).
95. B. Blonder *et al.*, hypervolume: High dimensional geometry, set operations, projection, and inference using Kernel density estimation, support vector machines, and convex hulls (2025). https://github.com/bblonder/hypervolume. Accessed 26 October 2025.
96. W. Brightly, C. T. Stayton, convevol: Analysis of convergent evolution (2024). https://CRAN.R-project.org/package=convevol. Accessed 26 October 2025.
97. D. M. Grossnickle *et al.*, Challenges and advances in measuring phenotypic convergence. *Evolution* **78**, 1355–1371 (2024).
98. M. Pennell *et al.*, geiger v2.0: An expanded suite of methods for fitting macroevolutionary models to phylogenetic trees. *Bioinformatics* **30**, 2216–2218 (2014).
99. D. L. Rabosky *et al.*, Analysis and visualization of complex macroevolutionary dynamics: An example from Australian scincid lizards. *Syst. Biol.* **63**, 610–627 (2014).
100. R. A. Folk *et al.*, Rates of niche and phenotype evolution lag behind diversification in a temperate radiation. *Proc. Natl. Acad. Sci. U.S.A.* **116**, 10874–10882 (2019).
101. A. Liaw, M. Wiener, Classification and regression by randomForest. *R News* **2**, 18–22 (2002).
102. W. K. Kremers, N. B. Larson, glmnetr: Nested cross validation for the relaxed lasso and other machine learning models (2025). https://CRAN.R-project.org/package=glmnetr. Accessed 30 October 2025.